https://doi.org/10.1016/j.jallcom.2019.06.268

Atomistic understanding of deformation-induced heterogeneities in wire drawing and their effects on the tensile ductility of metallic glass wires

Lei Zhao [a], Kangcheung Chan [a, *], Shidong Feng [a], Xianzheng Lu [a], Shunhua Chen [b], Gang Wang [c]

[a] *Advanced Manufacturing Technology Research Centre, Department of Industrial and Systems Engineering, The Hong Kong Polytechnic University, Hung Hom, Kowloon, Hong Kong*

[b] *School of Mechanical Engineering, Hefei University of Technology, Hefei 230009, China*

[c] *Laboratory for Microstructures, Institute of Materials, Shanghai University, Shanghai 200444, China*

Submitted to

Journal of Alloys and Compounds

As a full paper

∗ Correspondence authors.

E-mail address: kc.chan@polyu.edu.hk (K.C. Chan)

Abstract

Compared to crystalline metals, metallic glasses (MGs) show an exceptional feature of improved ductility after being mechanically processed by wire drawing. However, its underlying mechanisms have not yet been fully elucidated. In this study, with the aid of atomistic simulations, wire drawing and subsequent tensile loading were performed on MG nanowires to systematically investigate the deformation mechanisms of MGs in wire drawing, the deformation-induced heterogeneities and their influences on the tensile ductility. The results revealed that the deformation mechanisms of MGs in wire drawing are closely associated with the area reduction ratio (R): at a small R of 4.7%, the area reduction is realized via shear transformations of atoms near the surface, leaving the core intact; while at a large R of 9.3%, it relies on the formation of multiple spatially distributed shear bands that redistributes the plasticity throughout the sample. The deformation-induced heterogeneities were understood through the detailed analysis of the resultant residual strain and stresses, the gradient rejuvenated amorphous structures, the unique free volume distribution and spatially distributed shear bands. Moreover, the tensile simulations revealed improved ductility synchronized with decreased yield strength of the drawn samples. The improved ductility is attributed to the synergistic effects of three beneficial factors: 1) The surface compressive residual axial stress leads to a shift of the yield sites from the surface to the core, suppressing the rapid formation of shear bands; 2) The rejuvenated structures near the surface constrain and accommodate the plastic deformation in the core; 3) The spatially distributed shear bands, generated at large R, serve as heterogeneous nucleation sites for highly dispersed plastic shearing. The findings provide a comprehensive elucidation of the deformation-induced heterogeneities of MGs in wire drawing and establish a physical relationship between these heterogeneities and mechanical properties, which can serve to interpret the experimental results.

Keywords: Metallic glass; Wire drawing; Deformation-induced heterogeneities; Tensile ductility; Molecular dynamics

1. Introduction

Metallic glasses (MGs), regarded as a type of promising “green” materials, have drawn extensive attention because of their high elasticity and strength, high fracture toughness and remarkable hardness [1, 2]. However, most MGs under deformation at room temperature are susceptible to strain localization, which results in limited plasticity before failure [3, 4]. The brittleness seriously restricts their potential utilization as structural materials [3-5]. It is argued that proper plastic pre-deformation can introduce inhomogeneous characteristics over the amorphous matrix, e.g., microstructural and stress fluctuation or gradient, which are beneficial for ductilizing MGs [6-8]. Recently, a variety of mechanical pretreatments drawn from the experience of processing crystalline metals were performed on MGs to improve their overall mechanical properties. In comparison with the composition adjustment method, these extrinsic mechanical pretreatments are insensitive to the composition and have unparalleled simplicity in processing. For instance, surface mechanical attrition treatment was successfully applied on CuZrAlTi MGs to induce gradient amorphous structures and compressive residual stress on the sample surface, through which an unusual work-hardening phenomenon and improved tensile ductility were observed [8]. Channel-die compression performed on Zr-based MGs was also demonstrated to introduce heterogeneous microstructures comprised of soft and hard regions, as revealed by large hardness fluctuation, which leads to an improvement of plasticity under compression [9]. Meanwhile, MGs processed by cold-rolling exhibited obvious plasticity due to the competitive activation of pre-existing shear bands in different orientations [7]. Attempts have been also made to optimize the mechanical properties of MGs using equal channel angular pressing [10], shot-peening [11] and high-pressure torsion [12], etc.

Among various mechanical pretreatments, the wire drawing process has attracted great attention since it is a highly controllable and precise technique for successively processing small-sized MG wires at room temperature. It has been reported that Pd-, Fe- and Co-based MG wires could be drawn to a total area reduction ratio (R) as high as 75~93% by selecting

appropriate *R* per step [13-15]. More importantly, the cold-drawn MG wires exhibited excellent surface quality and precisely controlled dimensions with high uniformity [13, 16], both of which are of significance in many practical applications such as microelectromechanical systems (MEMSs) and sensors [17]. Wire drawing has also been proven to have a remarkable influence on the mechanical and functional properties due to the deformation-induced heterogeneities [13, 14, 16]. For instance, Takayama et al. [14] reported that drawn Pd-based MG wires exhibit considerably increased elongation combined with fracture stress 8% higher than the undrawn wires. The enhanced mechanical properties were speculated to result from the interactions between pre-existing shear bands generated in wire drawing. Wu et al. [13] found that, below a total *R* of 22%, a synchronized improvement of the tensile ductility and fracture strength was achieved in drawn Co-based MG wires by eliminating defects and compositional nonuniformity, accompanied by producing compressive residual stress on the surface. While, upon exceeding the critical *R* of 22%, the fracture strength decreases due to the deformation-induced loose packing atomic structures and flow defects that soften the wires. Wang et al. [16] also revealed an enhanced tensile plasticity of 1.64% and ultimate tensile strength exceeding 4 GPa for drawn Co-based MG wires. Moreover, they found that wire drawing could improve the giant magneto-impedance effect, which was attributed to the generation of deformation-induced nanocrystals and circumferential and longitudinal residual compressive stresses. These pioneering experimental studies have given significant insights into the effects of wire drawing on the material properties of MG wires.

It is also noted that such experimental understanding of the deformation-induced residual stress and microstructure change of small-sized MGs in wire drawing, as well as their effects on the mechanical behaviour, is still phenomenologically based. The obstacle mainly arises from the difficulty in quantitatively detecting the subtle variations of the amorphous structures and stresses through various experimental methods, such as transmission electron microscope observation and X-ray diffraction analysis, due to the disordered atomic configuration of MGs

[18, 19]. Systematic evaluation of the spatial distributions of atomic structures and stresses in small-sized MG wires is far more challenging. In the literature, there has been a wide range of investigations on wire drawing in processing crystalline metals, and the deformation mechanisms have been comprehensively uncovered [20-22]. However, due to the intrinsic difference in the atomic structures, the deformation mechanisms and structural evaluations, as found for crystalline metals, should not be applicable for MGs in wire drawing. So far, the deformation mechanisms of MGs in wire drawing, the resultant structure and stress signatures as well as their effects on the mechanical properties, are still far from clear and worthy of further investigation. Molecular dynamics (MD) simulation, which enable one to directly explore the detailed plastic deformation behaviour at the atomic level, and to effectively investigate the temporal and spatial evolutions of amorphous structures and internal stresses of MGs under complex deformation conditions that are not assessable experimentally to date, is an useful tool to probe this issue [23-25]. So far, MD simulations have been successfully adopted to investigate the structural evolution and mechanical responses of MGs under shock waves [19], surface severe plastic deformation [26] and high-pressure torsion [27]. To the authors' knowledge, no attention has been given to understand the deformation-induced heterogeneities in wire drawing and their effects on the ductility of MGs using MD simulations.

In this study, wire drawing, as a mechanical pretreatment for processing small-sized MG wires in experimental studies, was innovatively reproduced on MG nanowires using large-scale MD simulation. The atomistic deformation mechanisms of MG nanowires in wire drawing, the origin of deformation-induced structural and stress heterogeneities as well as their influences on the tensile ductility under subsequent tensile loading are systematically investigated at the atomic level. It is shown that although the MD simulations are limited to small sample sizes, the models are sufficient to capture the deformation essences of MGs in wire drawing. This work is intended to provide a comprehensive elucidation of the deformation-induced heterogeneities of MGs resulting from the inhomogeneous plastic deformation in wire drawing,

and to establish a physical relationship between the deformation-induced heterogeneities and the enhanced tensile ductility observed in experiments.

2. Simulation methods

Large-scale MD simulations were performed on LAMMPS [28] using the embedded-atom-method potential developed by Sheng et al. [29]. A constant time step of 2 fs was adopted for all simulations. The original $Cu_{64}Zr_{36}$ MG nanowire, with dimensions of ϕ 42.0 nm × 92.0 nm (diameter × length), contains about 8 million atoms. Its primitive structure was prepared by quenching a small $Cu_{64}Zr_{36}$ melt (30,000 atoms) from a homogenization temperature of 2000 K to 100 K at a quenching rate of 1×10^{10} K/s. A constant-pressure-temperature ensemble (NPT) was adopted and periodic boundary conditions (PBCs) were imposed in three dimensions. The as-quenched glass was further replicated to form a much larger one, followed by bulk cutting to the dimensions of the original MG nanowire. The freshly cut sample was subsequently kept at 100 K for 0.1 ns using a constant-volume-temperature ensemble (NVT).

Fig. 1 displays the schematic diagram of wire drawing adopted in this study. The dies used in experiments were viewed as rigid bodies and represented by several prime working surfaces of the orifices (shown in yellow). More specifically, the entrance and back relief were simplified into two truncated conical surfaces, which were connected by an intersecting cylindrical surface (i.e., the bearing section). The semi-angles of the orifices (8° and 15°, respectively) were chosen according to the experimental study conducted by Wu et al. [13], while other length-related dimensions, such as the bearing length (12 nm), were roughly ascertained by downscaling the sizes from the realistic microscale to the MD nanoscale. In the implementation of the wire drawing simulations, the orifices were virtually defined as interior bounding walls which interact with nearby atoms of the samples, following the standard 12/6 Lennard-Jones potential ($\varphi_{LJ}(r)=4\bar{\varepsilon}\left[(\bar{\sigma}/r)^{12}-(\bar{\sigma}/r)^{6}\right], r<r_c$) [30], where r is a variable which describes the shortest distance between the atoms and the bounding walls. The bond energy

parameter ($\bar{\varepsilon}$), the bond length parameter ($\bar{\sigma}$) and potential cut-off radius (r_c) were chosen as 0.151 eV, 2.7 Å and 6.75 Å, respectively [31]. The original MG nanowire was one-pass drawn using dies with different inner diameters (D_m) of 41.5 nm, 41.0 nm, 40.5 mm and 40.0 nm, which correspond to a series of R ($R = (D_0^2 - D_m^2)/D_0^2$, where D_0 is the original diameter) of 2.4 %, 4.7%, 7.0% and 9.3%, respectively. A deformation temperature of 100 K was selected to alleviate thermodynamic fluctuations, highlighting the deformation behaviour of MGs in response to mechanical loading [32]. The drawing operation was realized by alternately shifting the right end (10 Å in thickness, shown in red) along the axial direction with a displacement of 0.08 Å each time, followed by relaxing the sample for 800 fs under the NVT ensemble. This results in an equivalent drawing speed of 10 m/s, a value two orders of magnitude lower than the sound speed in MGs (2.3 ~ 2.9 km/s) [3].

After being fully drawn, the samples were cut into lengths with a constant aspect ratio of 2.0, and further relaxed at 100 K for 0.2 ns. Tensile simulations were conducted on the drawn samples along the axial direction at an equivalent strain rate around 1×10^8 s^{-1}. The tensile movement was implemented by periodically displacing the rigid atoms at the two ends (10 Å in thickness) of the samples in backward directions. The temperature was maintained at 100 K under an NVT ensemble and free surfaces were set in the Y- and Z-directions. In this study, the simulation systems were smaller than the real experiments to accommodate the computational efficiency. While, as is demonstrated below, the adopted models were sufficient to capture the deformation mechanisms that are instrumental in understanding the experimental findings.

3. Results and discussion

3.1. Wire drawing of MG nanowires

3.1.1. The deformation mechanisms of MGs in wire drawing

Fig. 2 and Fig. 3 display the cross-sectional deformation patterns of two representative MG nanowires that were one-pass drawn with R of 4.7% and 9.3%, respectively. The deformation process was examined using the local atomic shear strain, η^{Mises} [33]. In general,

regions mapped with $\eta^{Mises} > 0.2$ indicate collective rearrangements of atomic clusters under stress and can be viewed as materials involved in shear transformation zones (STZs) [34]. One can see that the MG nanowires underwent a loading and unloading process of radical squeeze that arose from the interaction between the material and the orifice, and therefore deformed plastically. The diameters of the drawn MG nanowires were thus reduced, though with their final values a little larger than that of the orifices due to elastic recovery. Their lengths were elongated to accommodate the radial cross-sectional area reductions.

The spatial distributions of η^{Mises} in the two drawn MG nanowires clearly reflect a characteristic of deformation inhomogeneity and reveal *R*-dependent plastic deformation mechanisms in wire drawing. For the MG nanowires being drawn with a small *R* of 4.7% (Fig. 2), the area reduction was realized through local plastic deformation, which was prevailingly concentrated around the circumferential surface via activation of multiple STZs. In the core of the MG nanowire, although a certain amount of atomic rearrangements was triggered when the material was pulled through the orifice, the deformation was reversible after releasing from the back relief, thus leading to negligible inelastic deformation in the core (Fig. 2(c)-(d)). While, for the MG nanowire being drawn with the highest *R* of 9.3% (Fig. 3), besides abundant STZs induced near the surface, multiple shear bands were generated. These shear bands initiated from the surface and extended to the core with an average propagation angle of approximate 48° relative to the drawing direction. Meanwhile, they were inclined to cease propagation once the corresponding part of the materials was fully pulled through the bearing section. It is worth noting that they were spatially conical in shape and periodically arrayed with an average interval of 12 nm along the drawing direction (Fig. 3(b) and Fig. 3(d)). This characteristic of the shear band patterns obtained in MGs through the wire drawing process is quite different from those observed under uniaxial loadings, in which cases individual shear bands are generally parallel and constrained within narrow two-dimensional shear planes (Thus, they are more unstable for further plastic shearing upon loading) [35, 36]. In the MG nanowire drawn

with R = 9.3%, there was no perceptible shear offset or crack found on the circumferential surface (Fig. 3(d)), which clearly reflects the deformation stability of MGs in the wire drawing process. This finding is consistent with the experimental observations of the flawless and smooth surfaces of heavily drawn MG wires [13, 16, 37]. To examine whether the loading path influences the intrinsic mechanism of shear band-mediated deformation, one MG nanowire was also drawn to the same R of 9.3%, but through two passes with an R of around 4.7% per step. The deformation process of the second pass monitored by η^{Mises} (See Fig. S1 in Supplementary Material) shows a similar shear band patterns as observed in Fig. 3. This indicates that the loading path has no remarkable influence on the mechanism of shear band-mediated deformation in the MG nanowire. From these analyses, one can recognize that the plastic deformation of MG nanowires in wire drawing with a large R is characterized by the successive and stable generation of multiple three-dimensional shear bands.

In the literature, several experimental works [13, 14, 16] reported that MG wires can be drawn to a large accumulated R, as high as 64% ~ 93%, similar to malleable crystalline metals, through multi-pass drawing with a moderate R per step. It is noted that the diameters of MG wires adopted in experiments are usually in micro size (50 μm ~ 250 μm) and the diameter reduction per step is controlled within several micrometres, both of which are three orders of magnitude higher than those adopted in this MD study. Generally, reducing the characteristic sizes of MGs to the nanometre range tends to improve their plastic deformability and may even lead to shifted deformation modes, as revealed by various experimental and computational studies [38-41]. In this sense, the observation of shear band-mediated deformation behaviour in wire drawing of MGs using nanowires is expected to be more difficult than using microwires. Yet, as demonstrated in this atomistic study, the plastic deformation of the MG nanowire drawn with a large R of 9.3% relies on the successive and stable generation of spatially distributed shear bands. Therefore, it is reasonable to expect that the same deformation mode could take place for MG microwires in experiments. Following this viewpoint, one can speculate that

luxuriant and three-dimensional embryonic shear bands could be induced in the interior of experimental MG microwires after a heavy multi-pass drawing.

3.1.2. The origin of stable plastic deformation of MGs in wire drawing

As elaborated above, the plastic deformation of MGs in wire drawing is a successive and stable process of plastic flow. The plastic flow might be able to eliminate the superficial flows, if any, existing on the surface, a phenomenon has been verified in the experiments [13, 16]. This deformation behaviour is quite different from the cases under uniaxial loading. It is instructive to find the origin of stable plastic deformation behaviour of MGs in wire drawing. It is accepted that, for MGs that undergo uniform tensile stress states, once an embryonic shear band nucleates on the surfaces, it tends to propagate unimpeded across the whole sample, leading to the catastrophic failure soon after yielding [35, 42]. However, MGs suffer from multiaxial stresses, especially stresses in compressive states, tend to show more plastic deformability, as corroborated by many studies [43, 44]. The nonuniform distribution of stress in compressive states not only affects the formation of shear bands but also slows down the shear band dynamics [45]. So far, the stress states in the wire drawing process of crystalline metals have been extensively investigated using several approaches, such as X-ray diffraction, theoretical and finite element analysis [46-49]. Regardless of the kinds of materials being drawn, the samples can be roughly divided into two characteristic deformation zones, as schematically illustrated in Fig. 4(a), based on the internal stress states [49]. It is important to note that the surface materials (areas shown in red) in the region around the entrance is always under a state of high triaxial compressive stress, which arises from the resultant of the friction stress (τ_f) and the normal stress (σ_n) exerted by the orifice.

To verify this standpoint, the internal axial stress (σ_a), radial stress (σ_r) and circumferential stress (σ_c) distributions in the MG nanowire being drawn with R = 9.3% are examined. Their profiles along the radial direction (r) are displayed in Fig. 4(b). The stresses are calculated as follows: only atoms in the MG nanowire near the entrance (i.e., -5 nm ~ +5 nm around the

cross-section, A-A, shown in Fig. 3(a)) are reserved for statistical purposes. The atomic stress tensor of each atom ($\sigma_{\alpha\beta}^{k}$) is decomposed into three components in terms of the direction, i.e., σ_{axial}, σ_r and σ_c. The distribution of each term along the radial direction is then calculated by the formula: $\sigma_{\alpha\beta}(r)=\sum_{k=1}^{N(r)}\sigma_{\alpha\beta}^{k}\Big/\sum_{k=1}^{N(r)}V^{k}$, where $\sigma_{\alpha\beta}^{k}$ is the corresponding component of the atomic stress tensor of atom k, V^k is the Voronoi volume of atom k, and $N(r)$ is the corresponding atom number inside each binned concentric shell between r and $r + \Delta r$ from the central axis [50]. The bin size, Δr , is chosen to be 4.0 Å. The stresses in the tensile state are positive, whereas those in the compressive state are negative. It is seen from Fig. 4(b) that both the stress states in the core and the surface shell of the drawing MG nanowire are in accordance with the illustrations shown in Fig. 4(a). In the core of the drawing nanowire, an average σ_{axial} of 2.31 GPa was induced, a value reaching about 75% of the macroscopic yield stress, σ_y (σ_y = 3.07 GPa, as found in the subsequent tensile loading). This stress is the dominating stress component in the core of the MG nanowire as it is the driving force that pulls the sample through the orifice in wire drawing. While, as r closes to the surface shell, σ_{axial} changes to the reverse compressive state. Near the surface, σ_{axial} σ_r, and σ_c all become in a high compressive state, with their maximum values even surpassing σ_y. It is seen that, although the presence of the tensile stress is evident in the process of wire drawing, a state of high compressive stress is also induced near the surface. Bear in mind that the multiaxial compressive stress state is beneficial for plastic deformation of MGs. The steady plastic flow of MGs in wire drawing may be closely associated with the high triaxial compressive stress state near the surface [13, 16].

3.1.3. The residual strain and residual stresses after drawing

Due to the inhomogeneous plastic deformation, wire drawing also induces evident residual strain and residual stresses across the cross-section of the drawn wires [16]. To illuminate the spatial distributions of the residual strain and residual stresses after wire drawing, as an illustration, the profiles of the residual strain (measured by η^{Mises}) and residual stresses (measured by σ_{axial}, σ_r and σ_c) along the radial direction in the fully drawn MG nanowire with R = 4.7% are shown in Fig. 5(a)-(b), respectively. The residual strain at position r is taken as

the average values of η^{Mises} of those atoms located in the concentric shell between r and $r+\Delta r$ from the central axis. The residual stresses are obtained in the completely drawn MG nanowire in a similar way as mentioned in the previous section. With given σ_{axial}, σ_r and σ_c, the hydrostatic pressure, σ_{hp}, equals to $(\sigma_{axial}+\sigma_r+\sigma_c)/3$. Fig. 5(a) clearly reveals a characteristic of extremely inhomogeneous distributions of residual strain near the surface of the fully drawn MG nanowire. The depth of the severe deformation zone can be identified to be around 4.7 nm. This zone is in a triaxial compressive stress state, as can be seen from Fig. 5(b). It is noted that no matter in the core or near the surface of the drawn MG nanowire, σ_{axial} is the dominating residual stress component, with a value much larger than those of the other two components. σ_{axial} reaches a maximum value as high as -1.57 GPa in the surface region. To maintain the mechanical equilibrium in the axial direction, tensile stress is correspondingly induced in the core, with an average value of around 0.64 GPa. The hydrostatic pressure also illustrates a transition of the stress state from tension to compression as r increases from the core to the surface. It is worth noting that the same state of compressive residual stresses near the surface of drawn MG wires was confirmed by Wu et al. [13] via FE analysis, and Wang et al. [16] via theoretical modelling, and successfully adapted to interpret the R-dependent giant magneto-impedance and mechanical properties in experimentally drawn Co-based MG wires.

To better understand, or predict, the wire drawing process of MGs, Fig. 6(a) and Fig. 6(b) present the evolutions of the residual strain (η^{Mises}) and residual axial stress (σ_{axial}), respectively, in the MG nanowires drawn with four different Rs. The evolution of η^{Mises} shown in Fig. 6(a) clearly reveals a transition of the deformation mode from elastic deformation (R = 2.4% and 4.7%) to plastic deformation (R = 7.0 % and 9.3%) in the core of the drawn MG nanowires, which is in line with the results revealed in Fig. 2 and Fig. 3. The value of η^{Mises} at the same r increases as R increases from 2.4% to 9.3%, a manifestation of more severe plastic deformation under large R. Meanwhile, the characteristic of highly inhomogeneous plastic deformation is still observed in the cross-section even when the MG nanowire is heavily drawn. Fig. 6(b)

demonstrates that the surface is in a compressive residual stress state, regardless of different *R*s adopted in this study. The thickness of the surface shell that is in compressive residual stresses is enlarged gradually as *R* increases from 2.4% to 9.3%. However, the maximum amplitude of the compressive σ_{axial} near the surface does not follow the same trend but reaches the highest value when $R = 4.7\%$. The reduced compressive σ_{axial} in MG nanowires drawn with $R > 4.7\%$ may be attributed to the occurrence of plastic deformation in the core, which relieves the residual stress after mechanical equilibrium.

3.1.4. The gradient amorphous structures and unique free volume distribution after drawing

The inhomogeneous plastic deformation is also expected to induce gradient amorphous structures in the drawn samples, as experimentally evidenced by the obvious differences of the hardness and elastic modulus between the core and surface found by nanoindentation [13]. In this study, all the drawn samples are still fully amorphous without any evidence of structural ordering. To uncover the underlying structural changes, the structures of the drawn samples are analyzed in terms of topological short-range orders (SROs) using the Voronoi tessellation technique [35]. Based on the Voronoi analysis, a so-called five-fold symmetry parameter [51], defined as $f_5 = \sum_i f_5^i \times P_i$, is introduced as an overall structural indicator to characterize the structural evolution of MGs after wire drawing. Here P_i is the content of polyhedron type *i*, f_5^i represents the content of pentagons in polyhedron type *i* and is calculated via $f_5^i = n_5^i / N^i$, where N^i is the coordination number of polyhedron type *i* [51].

Fig. 7(a) shows the evolutions of f_5 in the series of drawn MG nanowires, along with its bulk value of the original MG nanowire for comparison. One can see that f_5 decreases remarkably in the materials near the surface that underwent severe plastic deformation. While, the changes are much smaller in the cores of the drawn samples, compared with the state prior to wire drawing. The distributions of f_5 clearly indicate a characteristic of gradient rejuvenated amorphous structures along the radial direction in the drawn MG nanowires, with the most disordered structural state near the surface. It is well recognized that five-fold symmetry favourable clusters, such as the closely packed icosahedral, constitute the skeleton of MGs

responsible for the strong-but-brittle behaviour of the glass [51, 52]. Plastic deformation destroys the icosahedral order of atomic clusters and induces irreversible structural disordering, causing degradation of local five-fold symmetry environment [52]. In this study, the evolution of f_5 along the radial direction clearly displays an opposite tendency relative to the spatial distribution of the residual strain shown in Fig. 6(a). This suggests that the gradient rejuvenated amorphous structure is closely associated with the strain gradient generated during wire drawing. The gradient rejuvenated amorphous structure promotes the microstructural fluctuations, which was found to be favourable to the tensile ductility of MGs [8, 53].

Fig. 7(b) demonstrates the distributions of the Voronoi volume (V_{Cu}) of the Cu atoms along the radial direction under different Rs. The relative volume change of the Voronoi polyhedral was used to evaluate the free volume change in the samples before and after drawing, similar to that in our previous work [53]. It is seen that, in comparison with the state prior to wire drawing, a net annihilation of free volume was observed near the surface for all the drawn MG nanowires, while a net generation was witnessed in the cores. It is argued that destruction of densely packed clusters in MGs under deformation could induce a certain degree of volumetric dilatation, resulting in a more access free volume and lower atomic packing density in the regions evolved in plastic deformation [32, 36]. In this sense, the free volume distribution observed in Fig. 7(b) appears to be inconsistent with the established consensus. However, it is noted that the remarkable residual stresses induced by wire drawing, as shown in Fig. 5(b) and Fig. 6(b), also affect the free volume distribution across the cross-section of the samples. A net annihilation of free volume near the surface is possible if the free volume contraction generated due to high compressive hydrostatic pressure exceeds the corresponding expansion triggered by the shear-driven dilatation. To rationalize the unique distribution of free volume, the MG nanowire drawn with R = 4.7% is illustrated as an example. It is seen from Fig. 7(b) that the average Voronoi volume of Cu atoms in the surface shell of the drawn MG nanowire contracts by 0.19%, while it expanded by 0.24% in the core. As mentioned above, the core of the drawn

MG nanowire is under elastic deformation. The volumetric change due to the residual stresses in the elastically deformed core can be roughly expressed as $\Delta V/V \approx \varepsilon_{axial} + \varepsilon_r + \varepsilon_c = 3\sigma_{hp}(1\text{-}2\nu)/E$, where ν is Poisson's ratio and E is Young's Modulus [54]. Given that ν = 0.36, E = 82 GPa for the $Cu_{64}Zr_{36}$ MG, and σ_{hp} = 0.21 GPa extracted from Fig. 5(b), the predicted $\Delta V/V$ is around 0.22%, a value which is in concordance with the average Voronoi volume change in the core. This result indirectly verifies the unique distribution of free volume in the drawn MG nanowires. It should be also emphasized that a net increase of free volume is still observed over the whole drawn MG nanowires.

As elaborated above, the MG nanowires processed by wire drawing demonstrate evident deformation-induced structural and stress heterogeneities, such as remarkable residual strain and residual stresses, gradient rejuvenated amorphous structures, unique free volume distribution, and even spatially distributed shear bands at large R. For clarity, Fig. 8 schematically summarizes the dominating deformation-induced heterogeneities in the MG nanowires drawn with different Rs, which may directly influence the plastic deformation behaviour and mechanical properties of the samples under subsequent loading [8, 11, 53, 55]. The original MG nanowire (i.e., R = 0) can be reviewed as a monolithic MG, due to the homogeneous "as-quenched" structure throughout the sample. While, arising from the local plastic deformation, the MG nanowire drawn with R = 4.7% is characterized by a high compressive residual axial stress combined with gradient rejuvenated amorphous structures in the surface shell, leaving the core in the elastic tensile state. Furthermore, for the MG nanowire drawn with the highest R = 9.3%, there exist multiple shear bands which were generated from the surface shell to the core, accompanied with the gradient rejuvenated amorphous structures and compressive residual axial stress in the surface shell.

3.2. Uniaxial tensile deformation of the drawn MG nanowires

With the wire drawing-induced heterogeneities established, we further turn our focus to examine how they influence the plastic deformation behaviour of the drawn samples under

subsequent tensile loading. So far, improved tensile ductility was reported in many wire drawing experiments on MGs [13, 14, 16, 37]. Nevertheless, the interpretations of the particular influences of wire drawing on the tensile ductility improvement of MGs in these experimental studies were still phenomenologically based and somewhat inconsistent. For instance, the experimental study conducted by Wang et al. [16] ascribed the enhanced ductility of Co-based MG wires to the deformation-induced precipitation of nanocrystals, which were believed to arrest the rapid propagation of shear bands. While, other studies [13, 14] found no evidence of crystallization in Co- and Pd-based MGs, and attributed the enhanced ductility to the elimination of surface imperfections and compositional nonuniformity and the interactions of multiple pre-existing shear bands. The underlying mechanism of the ductility enhancement of MGs after wire drawing is still not clear enough. In the following, through a detailed analysis of the atomistic plastic deformation behaviour of the drawn MG nanowires, one may expect to better understand the mechanisms that govern the enhanced tensile ductility of drawn MGs.

3.2.1. Brittle-to-ductile transition

Fig. 9(a) shows the tensile stress-strain curves for the drawn samples, together with that of the original one (R=0) for comparison. Fig. 9(b) depicts the evolutions of the peak stress (σ_p) and macroscopic yield strain (ε_p) as a function of R. σ_p is viewed as the critical stress required for macroscopic yielding at the critical strain of ε_p [55]. It is seen that ε_p and σ_p both decrease progressively as R increases from 0 to 9.3%. Previous studies [23, 53, 55] associated with plasticity enhancement of MGs by tailoring various amorphous structures found that ε_p is independent of the structural disordering state in MGs. It can be, therefore, inferred that the reduced ε_p is attributed to the residual stress in the drawn samples. The decrease of σ_p indicates a softening trend of the samples after wire drawing. Generally, mechanical pre-deformation, such as rolling and high-pressure torsion, reduces the local energy barriers required for atomic rearrangement, which shall lower the strength for yielding under subsequent loading [55].

For all the samples, the stress-strain curves display an apparent stress drop ($\Delta\sigma=\sigma_p-\sigma_f$) upon exceeding σ_p, followed by a relatively steady plastic flow, which corresponds to the flow stress (σ_f). Recent theoretical and simulation studies revealed that the value of σ_f reflects the flow strength of a deformed MG or the strength of the propagating shear bands, and the value of $\Delta\sigma$ corresponds to a change in mechanical response caused by shear localization and softening [35, 36]. Generally, the smaller the $\Delta\sigma$, the better the tensile ductility. $\Delta\sigma$ decreases gradually as R increases from 0 to 9.3%, a manifestation of a tendency of more stable macroscopic plasticity after wire drawing [23]. One can recognize that the original nanowire (R = 0) exhibits an abrupt stress drop upon macroscopic yielding. The abrupt stress drop is associated with the rapid formation and propagation of one dominating shear band and has been viewed as an apparent characteristic of poor plasticity in MGs [34, 56]. In sharp contrast, the MG nanowire drawn with the highest R of 9.3% in this study exhibits a much more stable plastic flow, an indication of ductile deformation. The stress-strain curves clearly illuminate that the tensile ductility of the MG nanowires can be improved by wire drawing. It should be also noted that, due to the limitation of computational capability, the aspect ratio of the samples for the uniaxial tensile simulations is limited to 2.0 in this study. It is expected that a higher aspect ratio may impede the transition in the drawn MG nanowires since the larger elastic energy release promotes more severe strain localization soon after the macroscopic yielding [34, 57].

3.2.2. Mechanisms for the brittle-to-ductile transition

A close observation on the tensile deformation processes of the drawn MG nanowires monitored by η^{Mises} indeed found a brittle-to-ductile transition. The deformation behaviour can be classified into three categories: (1) a brittle-like shear banding mode for R = 0 and 2.4%; (2) a collaborative mode between shear banding and necking behaviour for R = 4.7% and 7.0%; and (3) a ductile necking mode for R = 9.3%. It should be emphasized that such a transition of the deformation mode with varied R should not be related to the size-dependent plasticity after the cross-section area reduction in the wire drawing process, since the critical diameter required

for the pure shear banding mode in $Cu_{64}Zr_{36}$ MG nanowires was found to be as low as 10 nm ~ 20 nm [58], which is much smaller than that the sample sizes adopted in this study. Instead, the transition appears to be associated with the structural and stress heterogeneities induced in the wire drawing process. In the following, the two drawn MG nanowires (R = 4.7% and 9.3%) together with the reference one (R = 0) are adopted to elucidate the effects of the deformation-induced heterogeneities on the brittle-to-ductile transition in the drawn MG nanowires under uniaxial tensile loading.

Fig. 10 presents a sequence of the cross-sectional snapshots of η^{Mises} for the three drawn MG nanowires at different applied strains. It should be noted that η^{Mises} here is evaluated by comparing the atomic configurations between the deformed state and the state prior to tensile loading rather than the state prior to wire drawing. As such, one can evaluate the process of plastic deformation that is directly induced by tensile loading. To illuminate the effects of the drawing-induced structural and stress heterogeneities on the tensile deformation behaviour of the drawn MG nanowires, Fig. 11(a)-(c) depicts the evolutions of the internal axial stress, σ_{axial}, along the radial direction of the samples at different applied strains. Concomitantly, Fig. 11(d)-(f) demonstrates the distributions of the resultant strain, η^{Mises}.

For the undrawn MG nanowire, due to the homogeneous "as-quenched" structure, σ_{axial} and η^{Mises} are almost evenly distributed in the sample before macroscopic yielding (ε_p = 6.4%), as shown in Fig. 11(a) and Fig. 11(d). A thin surface layer undergoes relatively large deformation since atoms near the surface are highly energetic, and more vulnerable to earlier irreversible shear transformations upon loading [35]. After the elastic deformation stage, several regions with large η^{Mises}, i.e., STZs, emerge on the surface (shown in black circles), which serve as nucleation sites for embryonic shear bands (see ε = 6.5% in Fig. 10(a)). With further loading, one of them grows and aggregates quickly, followed by the rapid generation and propagation of one dominating shear band across the sample. It is clear that the plastic

deformation and failure mode for the undrawn MG nanowire is dominated by highly localized shear banding (shown as the yellow line at ε = 18.0% in Fig. 10(a)). Moreover, the undrawn MG nanowire shows a strong tendency for the individual shear band to initiate from the surface. This phenomenon is consistent with the previous results found by Qu et al. [59] via experiments, and Cao et al. [35] via atomistic simulations on monolithic MGs.

Quite different deformation behaviour is observed for the two drawn MG nanowires that were endowed with different levels of stress and structural heterogeneities. It is seen from Fig. 11(b)-(c) that the distributions of σ_{axial} under uniaxial tensile loading are highly uneven in the pre-drawn MG nanowires, compared to that in the undrawn nanowire shown in Fig. 11(a). When the drawn MG nanowires are stretched, the compressive residual axial stress in the surface shell first counteracts the applied tensile stress at the early deformation stage, while the tensile residual axial stress in the core superimposes the applied tensile stress. This results in a smaller resultant σ_{axial} in the surface shell than in the core under uniaxial loading, which may lead to a shift of the initial yield sites from the free surface to the core in the drawn MG nanowires. The distributions of η^{Mises} shown in Fig. 11(e)-(f) indicate that the cores of the two drawn MG nanowires undergo larger deformation strains than in the surface shells around the macroscopic yield points (ε_p = 5.5% and 4.7% for the nanowires with R = 4.7% and 9.3%, respectively), which undoubtedly verifies the hypothesis of the shifted yielding sites.

A close observation on the deformation process found that, for the MG nanowire drawn with a moderate R of 4.7% (Fig. 10(b)), despite the fact that the surface shell was pre-rejuvenated and highly activated for plastic shearing, the growth of superficial STZs previously generated in wire drawing as well as the formation of new ones on the surface under tensile loading as observed in the undrawn MG nanowire are both suppressed at the early deformation stage, due to the existence of large residual compressive axial stress in the surface shell. Instead, plastic deformation first occurs in the core (see ε = 6.2% in Fig. 10(b)), which is initially in the

tensile stress state. In light of the unique deformation characteristics under uniaxial tension, the drawn nanowire with R=4.7% can be viewed as a glass-glass "core-shell" composite structure, but with the unrejuvenated hard core more prone to plastic deformation due to the existence of the high compressive residual stress in the surface shell. In the deforming "core-shell" amorphous structure, the plastic strain in the core and the surface shell must be accommodated during deformation. More specifically, after initial yielding in the core, the plastic deformation instability associated with the rapid formation of shear bands in the core can be constrained by the "elastically" pre-deformed material from the surface shell. As a consequent, STZs together with multiple embryonic shear bands (shown in white arrows) are developed in the core (see ε = 6.3% and 6.6% in Fig. 10(b)). With further loading, these embryonic shear bands interact with each other and deform in a cooperative manner, resulting in a mixed mode of shear banding and necking behaviour as observed at ε = 18.0% in Fig. 10(b).

For the MG nanowire drawn with the highest R of 9.3% adopted in this study, prior to the tensile loading, there exist abundant spatial distributed shear bands in the core as revealed in Fig. 3. Therefore, in comparison with the case of R = 4.7%, the heavily drawn MG nanowire can also be viewed as a similar glass-glass "core-shell" composite, but with multiple pre-existing embryonic shear bands and higher tensile residual stress existing in the core. It is seen from Fig. 10(c) that the activation of STZs in the surface shell is also suppressed due to the compressive residual axial stress, similar to the case for R = 4.7%. While, plastic deformation occurs in the core via a relatively uniform distribution of STZs (see ε = 6.0% in Fig. 10(c)). This unique generation of STZs may be attributed to the pre-existing multiple pre-existing shear bands in the core, which act as preferred nucleation sites for highly dispersed plastic shearing events under tensile loading [55]. One can also see that the density of STZs increases progressively under successive deformation without experiencing rapid aggregation. At large applied strains, this uniform plastic deformation in the core accommodates the plastic

deformation in the surface shell, which finally leads to much more homogenous-like necking deformation behaviour, as observed at ε = 18.0% in Fig. 10(c). The unique distribution of residual stress and microstructures promotes the redistribution of plasticity and dissipates more energy into a large volume of the sample, which is expected to alleviate the strain-induced softening associated with shear localization, thus giving rise to a much lower stress drop and higher flow stress, as observed in Fig. 9.

From the above analysis, one can recognize that the wire drawing process promotes the tensile ductility of MGs in three beneficial ways. Firstly, wire drawing induces high compressive residual axial stress in the surface shell, which may lead to a shift of the initial yield sites from the surface to the core. This reduces the likelihood of unstable shear banding behaviour associated with the rapid formation of one dominating shear band on the surface, promoting the formation of multiple embryonic shear bands in the samples after macroscopic yielding. The positive influence of compressive surface stresses on the plastic deformability has been well recognized in MGs processed via various surface pretreatment approaches, such as shot-peening [11], laser shock peening [60] and surface mechanical attrition treatment [8]. Even in the elastically pre-strained MGs obtained through elastostatic four-point bending, the compressive residual stresses were also found to promote the stable serrated flow and pile-up behaviour of MGs under nanoindentation [61]. Secondly, the wire drawing process produces gradient rejuvenated amorphous structures along the radial direction in the wire cross-section, which promotes the microstructural fluctuations within the samples. The rejuvenated amorphous structures in the surface shell serve as ductile phases, constraining the plastic deformation in the core and delaying the shear instability of the samples [53, 62]. Thirdly, the wire drawing process produces a high density of spatially distributed shear bands in the core at the largest R of 9.3%. Under subsequent tensile loading, the pre-existing shear bands act as heterogeneous nucleation sites for highly dispersed plastic shearing upon loading, which is expected to deliver more homogenous plastic deformation throughout the samples [55]. It

should be emphasized that the three factors are synergistically contributed to the tensile ductility improvement in the heavily drawn MG nanowire. Although each factor was individually verified to be beneficial to the plasticity of MGs in many experimental and computational investigations [53, 55, 61], it may not be easy to evaluate the dominating factor that governs the enhanced ductility in the heavy drawn MG nanowire. It should be also noted that various mechanical pretreatment techniques, such as shot peening [11] and surface mechanical attrition treatment [8], also produce similar deformation-induced structural and stress heterogeneities in MGs. The findings in this study should be also helpful in understanding the mechanical property changes in these experiments.

3.3. Amorphous structure vs. crystalline structure

Before concluding, it is instructive to compare the effects of the intrinsic atomic structures on the mechanical responses of materials after wire drawing. As revealed above, for amorphous metals, wire drawing leads to an improved tensile ductility and reduced yield strength, which is in accordance with previous experimental observations [8, 13, 14]. This is quite different in the case for crystalline metals, in which a reduced tensile ductility and improved yield strength are generally expected [63]. It should be noted that the well-established knowledge on wire drawing of crystalline metals cannot simply be used as a reference for amorphous metals due to their distinct atomic structures. There are two fundamental differences that prevent us from making a generalization for the two kinds of materials. Firstly, the plastic deformation of crystalline metals primarily relies on lattice dislocations and other lattice defects [20], while the plastic deformation of amorphous metals is associated with STZs, i.e., the elementary deformation units in the framework of the STZ model [64]. The different atomic structures are expected to result in distinct deformation mechanisms and microstructural evolutions [27]. More specifically, wire drawing increases dislocation concentrations in crystalline metals, which increase the resistance for further deformation due to dislocation pile-ups, a phenomenon known as strain hardening [63]. While, STZs and shear bands induced by wire drawing in

amorphous metals reduce the energy barriers of atoms for shear transformations, which give rise to lower strength for yielding, i.e., strain softening [55]. Secondly, the accumulated dislocations in cold-drawn crystalline metals act as barriers that dramatically impede their motion under subsequent tensile loading, which leads to a decrease of the tensile ductility. While, STZs and shear bands pre-existed in amorphous metals tend to serve as heterogeneous nucleation sites for highly dispersed plastic shearing, which delivers more plasticity [55]. The above comparisons provide a good explanation of the distinct differences in mechanical property changes between amorphous and crystalline metals observed in wire drawing experiments.

4. Conclusions

In this work, wire drawing and subsequent tensile loading were reproduced on MG nanowires using large-scale MD simulations. Valuable insights were gained into understanding the deformation mechanisms of MGs in wire drawing, the origin of deformation-induced heterogeneities and their influences on the tensile ductility from atomistic insights. The plastic deformation modes of MGs in wire drawing are found to be closely correlated with R: at small R, the area reduction is realized via shear transformations of atoms near the surface, leaving the core intact; while at large R, it relies on the formation of multiple spatially distributed shear bands that redistributes the plasticity throughout the sample. The steady plastic deformation during drawing is attributed to the high triaxial compressive stresses near the surface. Evident structural and stress heterogeneities, such as residual strain and stresses, gradient amorphous structures, unique free volume distribution and spatially distributed shear bands, were induced due to the highly inhomogeneous plastic deformation. Under subsequent tensile loading, these deformation-induced heterogeneities were found to lead to improved ductility and reduced yield strength of the drawn MGs. The ductility improvement is mainly ascribed to the synergistic effects of three beneficial factors: the high compressive residual axial stress near the surface, the gradient rejuvenated amorphous structures and the pre-existing spatially distributed shear bands. The reduced yield strength is attributed to the lower energy barriers required for atomic rearrangements after wire drawing. The findings not only provide a

comprehensive understanding on the deformation mechanisms of MGs in wire drawing and the relationship between the deformation-induced heterogeneities and mechanical properties, but also offer useful guidelines for processing MGs with desirable mechanical and functional properties.

Acknowledgements

This research was fully funded by the Research Committee of the Hong Kong Polytechnic University under research student project account code *RTLR*.

Supplementary Material

Supplementary data associated with this article can be found, in the online version, at….

References

[1] C.A. Schuh, T.C. Hufnagel, U. Ramamurty, Mechanical behavior of amorphous alloys, *Acta Mater.* 55(12) (2007) 4067-4109.

[2] A. Inoue, A. Takeuchi, Recent development and application products of bulk glassy alloys, *Acta Mater.* 59(6) (2011) 2243-2267.

[3] W.H. Wang, C. Dong, C.H. Shek, Bulk metallic glasses, *Mater. Sci. Eng., R* 44 (2-3) (2004) 45-90.

[4] S.H. Chen, K.C. Chan, L. Xia, Deformation behavior of a Zr-based bulk metallic glass under a complex stress state, *Intermetallics* 43 (2013) 38-44.

[5] A.L. Greer, Y.Q. Cheng, E. Ma, Shear bands in metallic glasses, *Mater. Sci. Eng., R* 74 (4) (2013) 71-132.

[6] H.B. Yu, J. Hu, X.X. Xia, B.A. Sun, X.X. Li, W.H. Wang, H.Y. Bai, Stress-induced structural inhomogeneity and plasticity of bulk metallic glasses, *Scripta Mater.* 61 (6) (2009) 640-643.

[7] J.W. Liu, Q.P. Cao, L.Y. Chen, X.D. Wang, J.Z. Jiang, Shear band evolution and hardness change in cold-rolled bulk metallic glasses, *Acta Mater.* 58(14) (2010) 4827-4840.

[8] Q. Wang, Y. Yang, H. Jiang, C.T. Liu, H.H. Ruan, J. Lu, Superior tensile ductility in bulk metallic glass with gradient amorphous structure, *Sci. Rep.* 4 (2014) 4757.

[9] S. Scudino, K.B. Surreddi, M.S. Khoshkhoo, M. Sakaliyska, G. Wang, J. Eckert, Improved

room temperature plasticity of Zr41.2Ti13.8Cu12.5Ni10Be22.5 bulk metallic glass by channel-die compression, *Adv. Eng. Mater.* 12(11) (2010) 1123-1126.

[10] C.M. Lee, K.W. Park, J.C. Lee, Plasticity improvement of a bulk amorphous alloy based on its viscoelastic nature, *Scripta Mater.* 59(8) (2008) 802-805.

[11] Y. Zhang, W.H. Wang, A.L. Greer, Making metallic glasses plastic by control of residual stress, *Nat. Mater.* 5(11) (2006) 857-860.

[12] S.H. Joo, D.H. Pi, A.D.H. Setyawan, H. Kato, M. Janecek, Y.C. Kim, S. Lee, H.S. Kim, Work-hardening induced tensile ductility of bulk metallic glasses via high-pressure torsion, *Sci. Rep.* 5 (2015) 9660.

[13] Y. Wu, H.H. Wu, X.D. Hui, G.L. Chen, Z.P. Lu, Effects of drawing on the tensile fracture strength and its reliability of small-sized metallic glasses, *Acta Mater.* 58(7) (2010) 2564-2576.

[14] S. Takayama, Drawing of Pd77.5Cu6Si16.5 metallic glass wires, *Mater. Sci. Eng.* 38(1) (1979) 41-48.

[15] M. Hagiwara, A. Inoue, T. Masumoto, Mechanical properties of Fe-Si-B amorphous wires produced by in-rotating-water spinning method, *Metall. Trans. A* 13(3) (1982) 373-382.

[16] H. Wang, F.X. Qin, D.W. Xing, F.Y. Cao, X.D. Wang, H.X. Peng, J.F. Sun, Relating residual stress and microstructure to mechanical and giant magneto-impedance properties in cold-drawn Co-based amorphous microwires, *Acta Mater.* 60(15) (2012) 5425-5436.

[17] M.M. Khan, A. Nemati, Z.U. Rahman, U.H. Shah, H. Asgar, W. Haider, Recent advancements in bulk metallic glasses and their applications: A review, *Crit. Rev. Solid State* 43(3) (2018) 233-268.

[18] K.K. Song, S. Pauly, Y. Zhang, S. Scudino, P. Gargarella, K.B. Surreddi, U. Kuhn, J. Eckert, Significant tensile ductility induced by cold rolling in Cu47.5Zr47.5Al5 bulk metallic glass, *Intermetallics* 19(10) (2011) 1394-1398.

[19] C. Ma, G.X. Wang, C. Ye, Y. Dong, Shocking of metallic glass to induce microstructure heterogeneity: A molecular dynamics study, *J. Appl. Phys.* 122(9) (2017) 095102.

[20] F. Yang, Y. Wang, J. Jiang, F. Fang, C. Ma, K. Zhao, W. Li, Stress evolution of cold-drawn pearlitic steel wire subjected to uniaxial tension, *Mater. Sci. Eng. A* 487(1) (2008) 468-472.

[21] A. Phelippeau, S. Pommier, T. Tsakalakos, M. Clavel, C. Prioul, Cold drawn steel wires-processing, residual stresses and ductility-part I: metallography and finite element analyses,

Fatigue Fract. Eng. Mater. Struct. 29(3) (2006) 243-253.

[22] A. Phelippeau, S. Pommier, I. Zakharchenko, R. Levy-Tubiana, T. Tsakalakos, M. Clavel, M. Croft, Z. Zhong, C. Prioul, Cold drawn steel wires-processing, residual stresses and ductility-Part II: Synchrotron and neutron diffraction, *Fatigue Fract. Eng. Mater. Struct.* 29(3) (2006) 255-265.

[23] Z.D. Sha, P.S. Branicio, H.P. Lee, T.E. Tay, Strong and ductile nanolaminate composites combining metallic glasses and nanoglasses, *Int. J. Plast.* 90 (2017) 231-241.

[24] D. Şopu, K. Albe, J. Eckert, Metallic glass nanolaminates with shape memory alloys, *Acta Mater.* 159 (2018) 344-351.

[25] L. Zhao, K.C. Chan, S.H. Chen, Atomistic deformation mechanisms of amorphous/polycrystalline metallic nanolaminates, *Intermetallics* 95 (2018) 102-109.

[26] C. Ma, S. Suslov, C. Ye, Y.L. Dong, Improving plasticity of metallic glass by electropulsing-assisted surface severe plastic deformation, *Mater. Design* 165 (2019) 107581.

[27] S.D. Feng, W. Jiao, Q. Jing, L. Qi, S.P. Pan, G. Li, M.Z. Ma, W.H. Wang, R.P. Liu, Structural evolution of nanoscale metallic glasses during high-pressure torsion: A molecular dynamics analysis, *Sci. Rep.* 6 (2016) 36627.

[28] S. Plimpton, Fast parallel algorithms for short-range molecular dynamics, *J. Comput. Phys.* 117(1) (1995) 1-19.

[29] Y.Q. Cheng, E. Ma, H.W. Sheng, Atomic level structure in multicomponent bulk metallic glass, *Phys. Rev. Lett.* 102(24) (2009) 245501.

[30] J.E. Jones, On the determination of molecular fields.-II. From the equation of state of a gas, *Proc. R. Soc. A* 106 (738) (1924) 463-477.

[31] Y. Yang, J. Luo, L. Huang, G. Hu, K.D. Vargheese, Y. Shi, J.C. Mauro, Crack initiation in metallic glasses under nanoindentation, *Acta Mater.* 115 (2016) 413-422.

[32] Y.Q. Cheng, A.J. Cao, E. Ma, Correlation between the elastic modulus and the intrinsic plastic behavior of metallic glasses: The roles of atomic configuration and alloy composition, *Acta Mater.* 57(11) (2009) 3253-3267.

[33] F. Shimizu, S. Ogata, J. Li, Theory of shear banding in metallic glasses and molecular dynamics calculations, *Mater. Trans.* 48(11) (2007) 2923-2927.

[34] D. Şopu, A. Foroughi, M. Stoica, J. Eckert, Brittle-to-ductile transition in metallic glass

nanowires, *Nano Lett.* 16(7) (2016) 4467-4471.

[35] A.J. Cao, Y.Q. Cheng, E. Ma, Structural processes that initiate shear localization in metallic glass, *Acta Mater.* 57(17) (2009) 5146-5155.

[36] S.D. Feng, L. Qi, L.M. Wang, S.P. Pan, M.Z. Ma, X.Y. Zhang, G. Li, R.P. Liu, Atomic structure of shear bands in Cu64Zr36 metallic glasses studied by molecular dynamics simulations, *Acta Mater.* 95 (2015) 236-243.

[37] L.A. Davis, Cold drawing of metallic glasses, *Scripta Metall.* 16(8) (1982) 993-994.

[38] X.L. Zhou, H.F. Zhou, X.Y. Li, C.Q. Chen, Size effects on tensile and compressive strengths in metallic glass nanowires, *J Mech. Phys. Solids* 84 (2015) 130-144.

[39] J. Yi, W.H. Wang, J.J. Lewandowski, Sample size and preparation effects on the tensile ductility of Pd-based metallic glass nanowires, *Acta Mater.* 87 (2015) 1-7.

[40] X. Wang, F. Jiang, H. Hahn, J. Li, H. Gleiter, J. Sun, J. Fang, Sample size effects on strength and deformation mechanism of Sc75Fe25 nanoglass and metallic glass, *Scripta Mater.* 116 (2016) 95-99.

[41] C. Zhong, H. Zhang, Q.P. Cao, X.D. Wang, D.X. Zhang, U. Ramamurty, J.Z. Jiang, On the critical thickness for non-localized to localized plastic flow transition in metallic glasses: A molecular dynamics study, *Scripta Mater.* 114 (2016) 93-97.

[42] Z.D. Sha, S.X. Qu, Z.S. Liu, T.J. Wang, H. Gao, Cyclic deformation in metallic glasses, *Nano Lett.* 15(10) (2015) 7010-7015.

[43] S.H. Chen, A. Domel, T.M. Yue, C.P. Tsui, K.C. Chan, K.A. Dahmen, P.K. Liaw, Deformation behavior of bulk metallic glasses under a mixed-mode (I/II) loading condition, *Intermetallics* 93 (2018) 148-154.

[44] J. Pan, Y.X. Wang, Y. Li, Ductile fracture in notched bulk metallic glasses, *Acta Mater.* 136 (2017) 126-133.

[45] B.A. Sun, S.H. Chen, Y.M. Lu, Z.G. Zhu, Y.L. Zhao, Y. Yang, K.C. Chan, C.T. Liu, Origin of shear stability and compressive ductility enhancement of metallic glasses by metal coating, *Sci. Rep.* 6 (2016) 27852.

[46] S.K. Lee, D.W. Kim, M.S. Jeong, B.M. Kim, Evaluation of axial surface residual stress in 0.82-wt% carbon steel wire during multi-pass drawing process considering heat generation, *Mater. Design* 34 (2012) 363-371.

[47] F. Yang, J. Jiang, F. Fang, Y. Wang, C. Ma, Rapid determination of residual stress profiles in ferrite phase of cold-drawn wire by XRD and layer removal technique, *Mater. Sci. Eng. A* 486(1) (2008) 455-460.

[48] L.K. Kabayama, S.P. Taguchi, G.A.S. Martínez, The influence of die geometry on stress distribution by experimental and FEM simulation on electrolytic copper wiredrawing, *Mater. Res.* 12(3) (2009) 281-285.

[49] B. Radi, A. El Hami, Material forming processes: simulation, drawing, hydroforming and additive manufacturing, John Wiley & Sons, 2016.

[50] Q. Zhang, Q.K. Li, M. Li, Internal stress and its effect on mechanical strength of metallic glass nanowires, *Acta Mater.* 91 (2015) 174-182.

[51] Y.C. Hu, F.X. Li, M.Z. Li, H.Y. Bai, W.H. Wang, Five-fold symmetry as indicator of dynamic arrest in metallic glass-forming liquids, *Nat. Commun.* 6 (2015) 8310.

[52] M.Z. Li, Correlation between bocal atomic symmetry and mechanical properties in metallic glasses, *J. Mater. Sci.Technol.* 30 (6) (2014) 551-559.

[53] L. Zhao, K.C. Chan, S.H. Chen, S.D. Feng, D.X. Han, G. Wang, Tunable tensile ductility of metallic glasses with partially rejuvenated amorphous structures, *Acta Mater.* 169 (2019) 122-134.

[54] X.D. Wang, S. Aryal, C. Zhong, W.Y. Ching, H.W. Sheng, H. Zhang, D.X. Zhang, Q.P. Cao, J.Z. Jiang, Atomic picture of elastic deformation in a metallic glass, *Sci. Rep.* 5 (2015) 9184.

[55] H.F. Zhou, C. Zhong, Q.P. Cao, S.X. Qu, X.D. Wang, W. Yang, J.Z. Jiang, Non-localized deformation in metallic alloys with amorphous structure, *Acta Mater.* 68 (2014) 32-41.

[56] C. Zhong, H. Zhang, Q.P. Cao, X.D. Wang, D.X. Zhang, U. Ramamurty, J.Z. Jiang, Deformation behavior of metallic glasses with shear band like atomic structure: A molecular dynamics study, *Sci. Rep.* 6 (2016) 30935.

[57] Z.D. Sha, L.C. He, S. Xu, Q.X. Pei, Z.S. Liu, Y.W. Zhang, T.J. Wang, Effect of aspect ratio on the mechanical properties of metallic glasses, *Scripta Mater.* 93 (2014) 36-39.

[58] Q. Zhang, Q.K. Li, M. Li, Processing dependence of mechanical properties of metallic glass nanowires, *Appl. Phys. Lett.* 106 (7) (2015) 071905.

[59] R.T. Qu, Z.Q. Liu, G. Wang, Z.F. Zhang, Progressive shear band propagation in metallic

glasses under compression, *Acta Mater.* 91 (2015) 19-33.

[60] Y.F. Cao, X. Xie, J. Antonaglia, B. Winiarski, G. Wang, Y.C. Shin, P.J. Withers, K.A. Dahmen, P.K. Liaw, Laser shock peening on Zr-based bulk metallic glass and its effect on plasticity: Experiment and modeling, *Sci. Rep.* 5 (2015) 10789.

[61] F. Haag, D. Beitelschmidt, J. Eckert, K. Durst, Influences of residual stresses on the serrated flow in bulk metallic glass under elastostatic four-point bending - A nanoindentation and atomic force microscopy study, *Acta Mater.* 70 (2014) 188-197.

[62] Y. Wang, M. Li, J. Xu, Free volume gradient effect on mechanical properties of metallic glasses, *Scripta Mater.* 130 (2017) 12-16.

[63] A.M. Habraken, Material forming processes, Kogan Page Science, London, 2003.

[64] A.S. Argon, Plastic deformation in metallic glasses, *Acta Metall.* 27(1) (1979) 47-58.

Caption

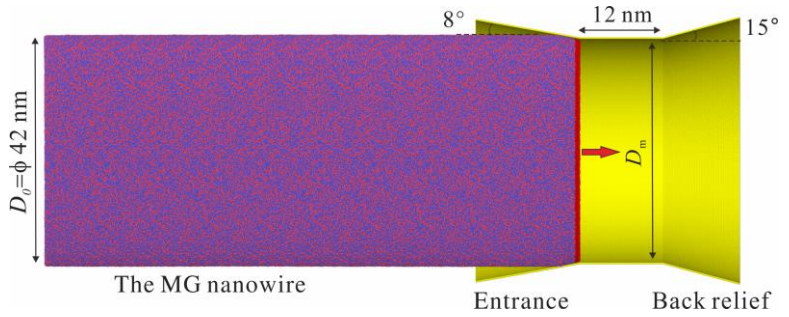

Fig. 1. Schematic illustration of the wire drawing process, in which the virtual die was visualized in yellow. The clamping part of the MG nanowire for the drawing movement was coloured in red. The blue and red atoms in the MG nanowire denote the Cu and Zr atoms, respectively.

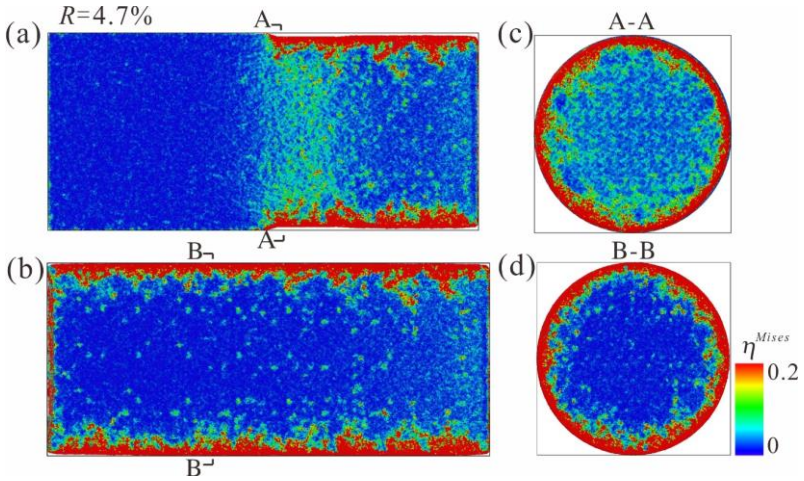

Fig. 2. Cross-sectional snapshots demonstrating the deformation process of the MG nanowire being drawn with R = 4.7%: **(a)** and **(b)** show the images that are parallel to the axial direction during drawing and after being fully drawn, respectively; **(c)** and **(d)** show the images that are perpendicular to the axial direction during drawing and after being fully drawn, respectively. The atoms are coloured according to their η^{Mises} values.

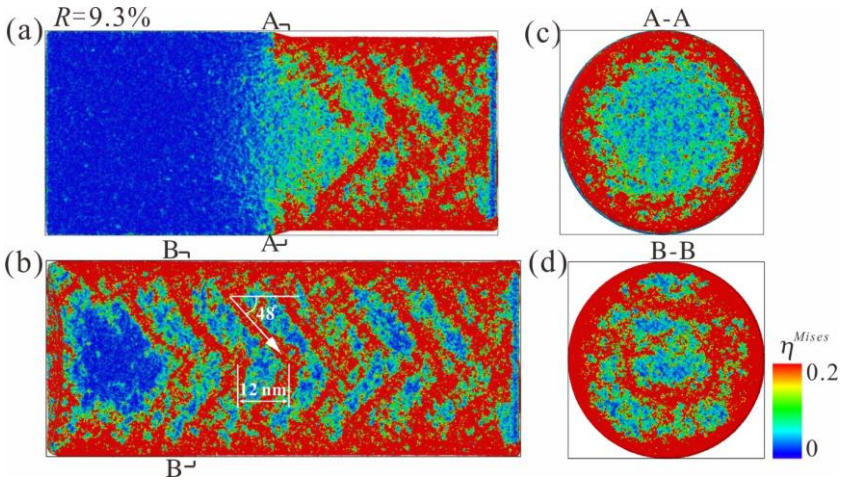

Fig. 3. Cross-sectional snapshots demonstrating the deformation process of the MG nanowire being drawn with R = 9.3%: **(a)** and **(b)** show the images that are parallel to the axial direction during drawing and after being fully drawn, respectively; **(c)** and **(d)** show the images that are perpendicular to the axial direction during drawing and after being fully drawn, respectively. The atoms are coloured according to their η^{Mises} values.

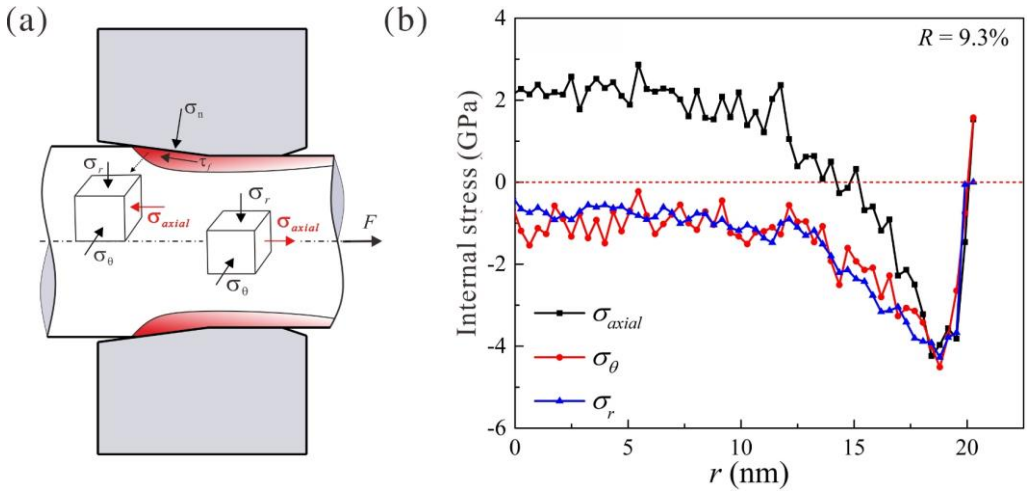

Fig. 4. (a) Schematic illustration of the stress states of the two characteristic deformation zones in wire drawing. F donates the external applied drawing force, while σ_n and τ_f around the entrance donate the resultant normal stress and friction stress, respectively. **(b)** The radial-direction profiles of the internal stresses, σ_{axial}, σ_c and σ_r, in the MG nanowire being drawn with R = 9.3%. The values of the X-coordinate refer to the location with respect to the central axis of the samples.

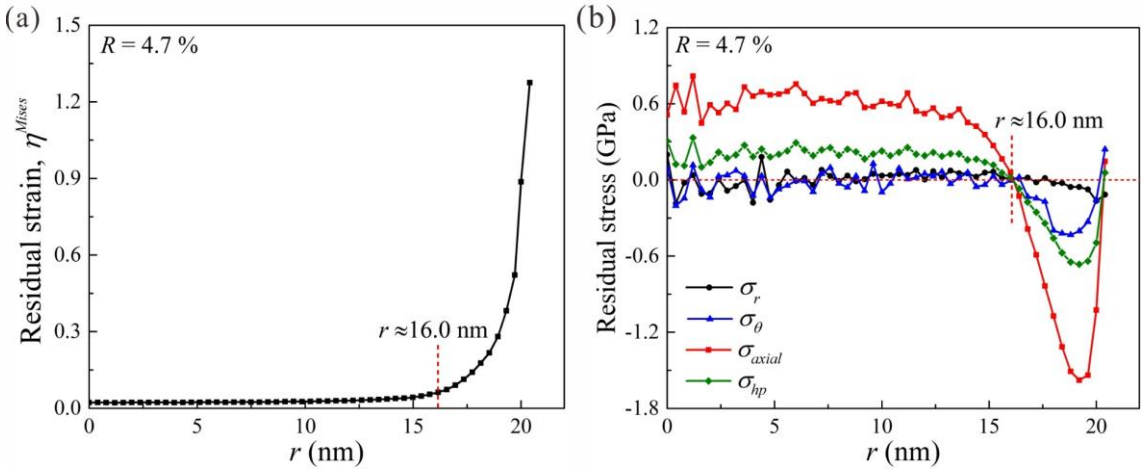

Fig. 5. The radial-direction profiles of **(a)** the residual strain (η^{Mises}) and **(b)** the residual stresses (σ_{axial}, σ_c, σ_r and σ_{hp}) in the MG nanowire drawn with R = 4.7%. The bin size for sampling, or the thickness of each concentric shell, is 0.4 nm.

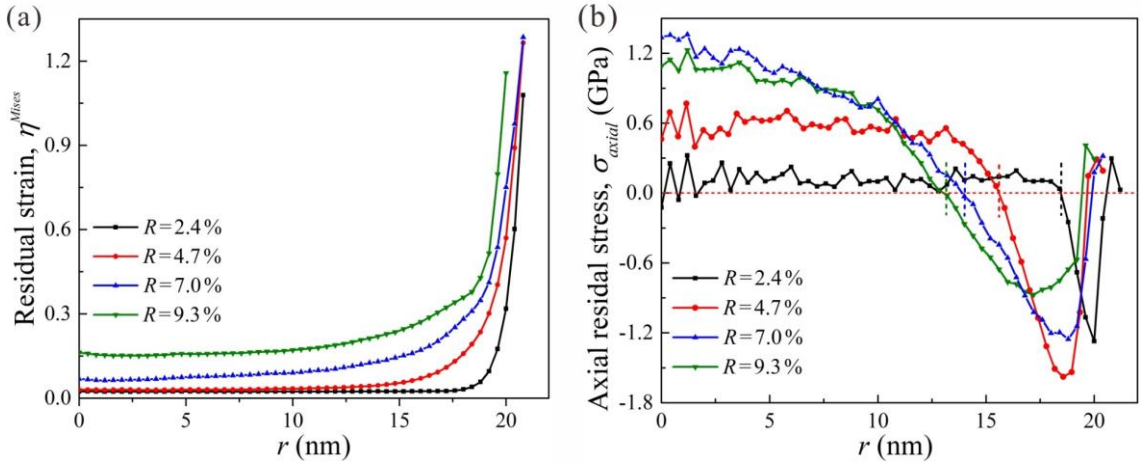

Fig. 6. The evolution of **(a)** the residual strain (η^{Mises}) and **(b)** the residual axial stress (σ_{axial}) under different *R*s in the fully drawn MG nanowires.

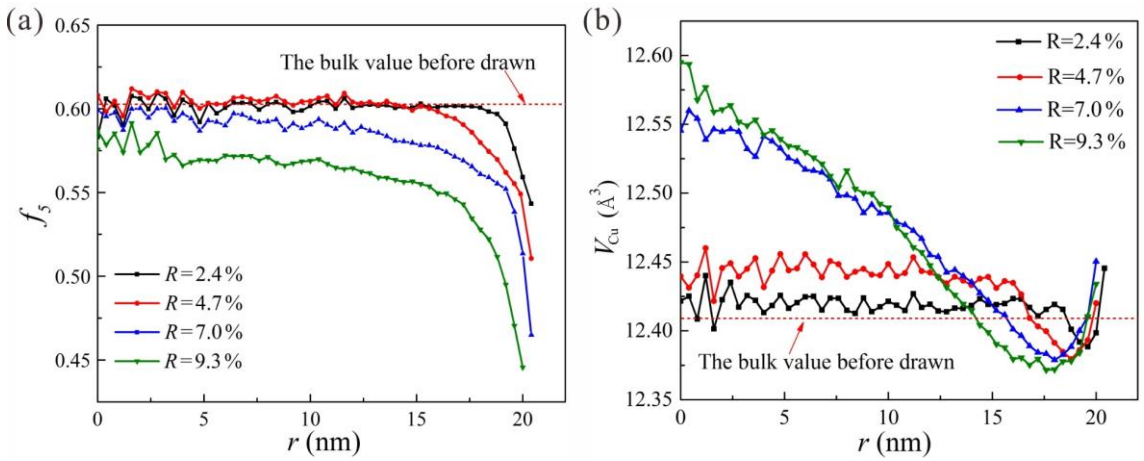

Fig. 7. The radial-direction profiles of **(a)** the five-fold symmetry parameter (f_5) and **(b)** the Voronoi volume of the Cu atoms (V_{Cu}), revealing the structural evolution in the drawn MG nanowires.

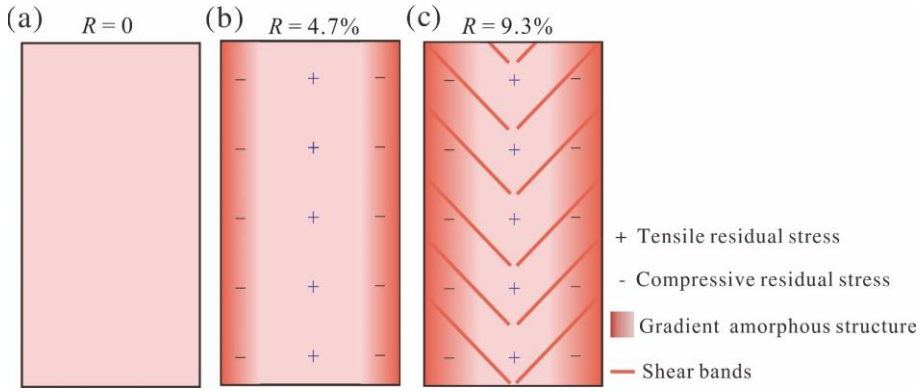

Fig. 8. Schematic illustration of the deformation-induced structural and stress heterogeneities in the MG nanowires drawn with different *R*s: **(a)** $R = 0$, **(b)** $R = 4.7\%$ and **(c)** $R = 9.3\%$.

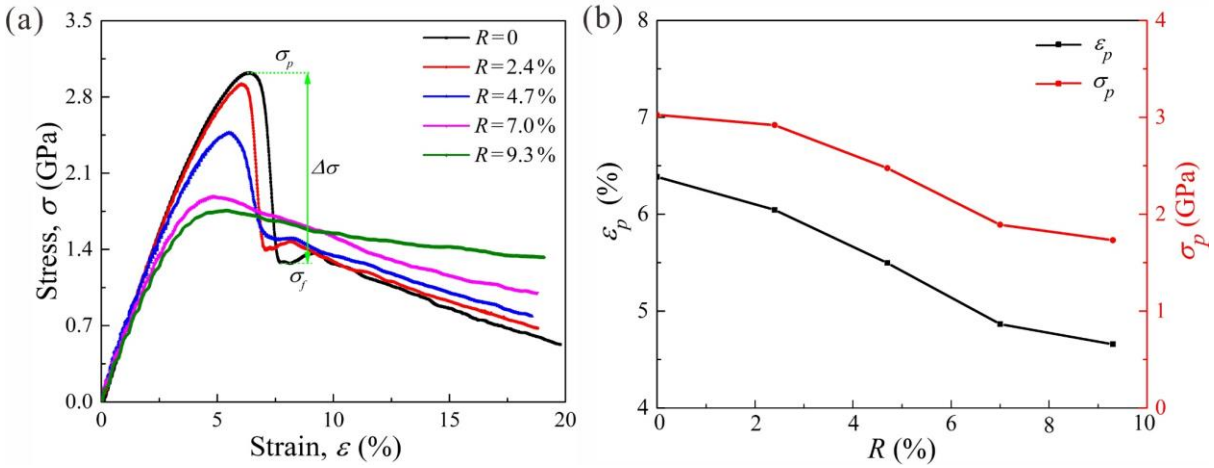

Fig. 9. (a) Uniaxial tensile stress-strain curves for the MG nanowires drawn with different *R*s; **(b)** the evolutions of ε_p and σ_p as a function of *R*.

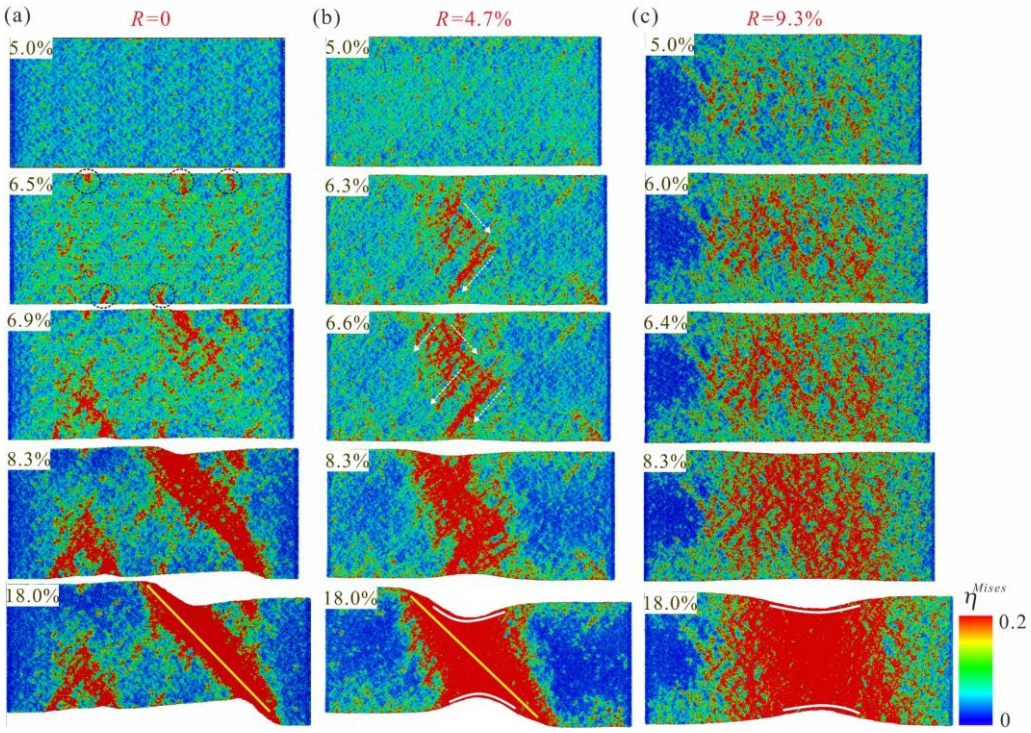

Fig. 10. Representative cross-sectional snapshots of η^{Mises} under uniaxial tensile loading for the MG nanowires drawn with different *R*s: **(a)** R = 0; **(b)** R = 4.7%; **(c)** R = 9.3%, demonstrating a transition of the deformation mode. Note that η^{Mises} here is evaluated by comparing the atomic configurations between the deformed state and the state prior to tensile loading. The yellow lines denote the shearing paths of shear bands, whereas the white ones represent necking profiles.

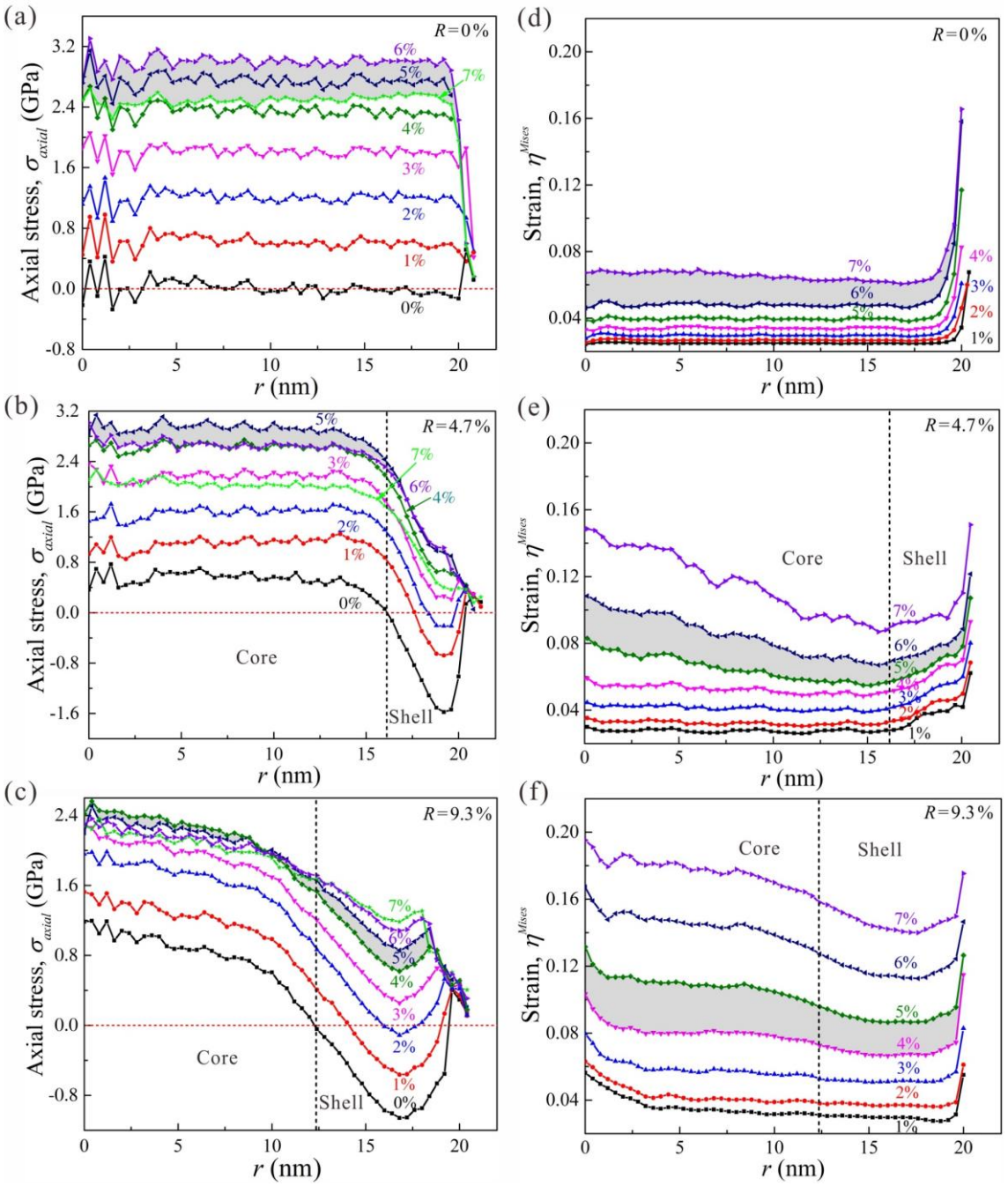

Fig. 11. The profiles of **(a)-(c)** σ_{axial} and **(d)-(e)** η^{Mises} along the radial direction at different applied strains under tensile loading for the MG nanowires drawn with different *R*s. The grey areas denote the strain ranges, in which macroscopic yielding occurs. The black dashed lines indicate the boundaries of the core and surface shell.

Supplementary Materials

Atomistic understanding of deformation-induced heterogeneities in wire drawing and their effects on the tensile ductility of metallic glass wires

Lei Zhao [a], Kangcheung Chan [a, *], Shidong Feng [a], Xianzheng Lu [a], Shunhua Chen [b], Gang Wang [c]

[a] *Advanced Manufacturing Technology Research Centre, Department of Industrial and Systems Engineering, The Hong Kong Polytechnic University, Hung Hom, Kowloon, Hong Kong*

[b] *School of Mechanical Engineering, Hefei University of Technology, Hefei 230009, China*

[c] *Laboratory for Microstructures, Institute of Materials, Shanghai University, Shanghai 200444, China*

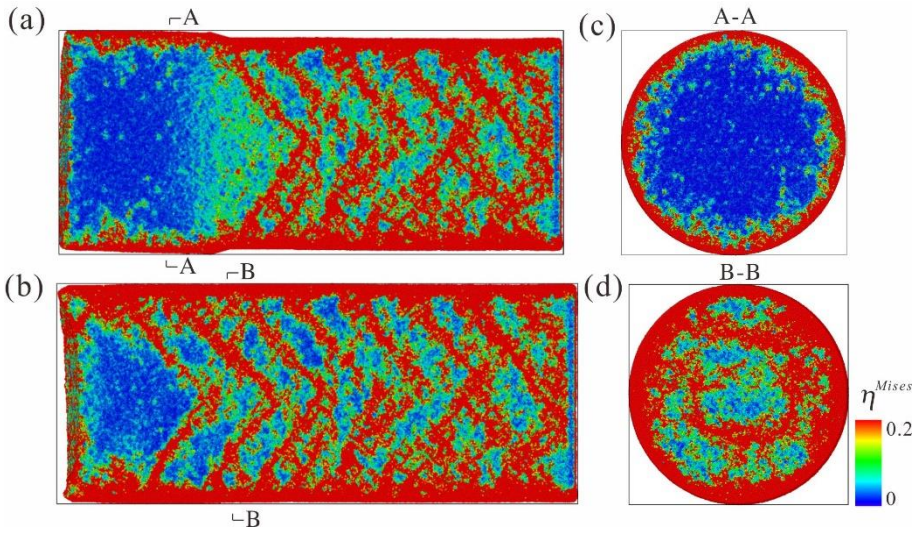

Fig. S1. The deformation process of the second pass of the MG nanowire being drawn with a total R = 9.3%: **(a)** and **(b)** show the images that are parallel to the axial direction during drawing and after being fully drawn, respectively; **(c)** and **(d)** show the images that are perpendicular to the axial direction during drawing and after being fully drawn, respectively. The atoms are coloured according to their η^{Mises} values.